Composite Structures 279 (2022) 114725

Contents lists available at ScienceDirect

Composite Structures

journal homepage: www.elsevier.com/locate/compstruct

An experimental investigation concerning the effect of AFP defects on progressive damage in CFRP coupons

Rafal Anay [a,*], Dennis Miller [b], Addis Tssema [b], Roudy Wehbe [b], Paul Ziehl [b], Brian Tatting [c], Zafer Gurdal [b], Ramy Harik [b], Addis Kidane [b]

[a] Department of Civil and Environmental Engineering, University of South Carolina, USA
[b] Department of Mechanical Engineering, University of South Carolina, USA
[c] McNair Center for Aerospace Innovation and Research, University of South Carolina, USA

ARTICLE INFO

Keywords:
Tensile coupon
Three-point bending
Acoustic emission
Signal strength
Intensity analysis

ABSTRACT

Manufacturing of composite laminates using the fiber placement process introduces the possibility of several types of defects and features that are not present in traditional hand-layup fabrication techniques. The effect of these defects on structural performance and failure has not been fully investigated, especially for those defects with small geometrical features. The innovation lies in using advanced methods to capture the effect of defects generated during manufacturing processes which can be used to determine if these defects warrant immediate repair to ensure part integrity. Several types and configurations of defects that may occur during the automated fiber placement (AFP) process were inserted within the coupons. Acoustic emission (AE) was employed as a nondestructive evaluation technique to investigate correlations between mechanical properties and damage propagation during tension and 3-point bending tests. Digital Image Correlation (DIC) was utilized to monitor damage progression in the bending test.

1. Introduction and objectives

Automated fiber placement (AFP) provides high quantity, efficient and precise manufacturing methods for producing laminated composites. It can be used for making flat and cylindrical structures and it has been employed in most engineering applications including aerospace, wind, oil & gas, pressure vessels, medical and sporting goods [8]. Moreover, major organizations such as Boeing, Airbus, and NASA have used AFP extensively for making highly precise components such as wing skins, nose cone fuselages and load-bearing propellant in future spacecraft [20,12,16,26]. During this manufacturing process, plies are laminated in a predesigned order and cured through an autoclave or infusion process [24]. This procedure is sensitive and macro-defects cannot always be avoided. Also, it can induce small random defects within the laminate, which may compromise the structural integrity [25].

Many types of composite manufacturing-induced defects may occur including resin-rich areas, voids, distorted fibers, broken/missing fibers, fiber misalignment, stacking sequence disorder, and inclusions [18,7,9,10]. These defects may increase the degradation rate of composite components and may cause failure at an earlier stage than expected. Specific to the AFP process, other defects may arise such as gaps, overlaps, wrinkles, folds, twists, bridging, splices, and others [19]. For instance, gaps and overlaps can be present in the design depending on the chosen layup strategy to achieve full coverage of a given complex surface [29]. However, they can also occur between adjacent tows or courses due to machine inaccuracy [19]. Twists in the tow material can be related to the machine rotations or inappropriately feeding the tows in the machine head [19]. Regarding tow wrinkles, they can occur due to excessive steering on flat or curved surfaces, and their existence can be related to the part geometry and the set of process parameters (temperature, compaction, layup speed) used during manufacturing [31,32,27]. In this paper, four specific types of defects, namely gaps, overlaps, twists and wrinkles between tows were selected based on four considerations including: a) uniqueness, b) method of introduction into the ply, either through programming or manual manipulation, c) ease of manufacturing at a coupon level, and d) additional parametric variables, such as size, shape, and orientation.

Several numerical and experimental studies have been conducted for detecting and evaluating defects in CFRP. Compressive failure of quasi-

* Corresponding author.
E-mail address: ranay@email.sc.edu (R. Anay).

https://doi.org/10.1016/j.compstruct.2021.114725
Received 9 November 2020; Received in revised form 25 August 2021; Accepted 23 September 2021
Available online 20 October 2021

Table 1
Laminate Definitions for Zero and Ninety Configurations.

Designation	Stacking Sequence	Defect Location	Layup/group Name
Zero	$[+45/90/-45/0]_s$	0-degree center ply	Zero configuration
Ninety	$[-45/0/+45/90]_s$	90-degree center ply	Ninety configuration

isotropic carbon–epoxy laminates containing an embedded wrinkle were investigated using experimental and numerical methods [22]. Extensive damage localization in the wrinkle region was observed using high-speed video of the gauge section. Moreover, 3D finite element (FE) simulations performed in Abaqus/Explicit were incorporated to capture the locations of damage and failure stress levels. It was concluded that the wrinkles significantly reduce the pristine compressive strength of the laminates. Depth determination of defects in CFRP-structures using lock-in thermography was introduced based on the complex wave field [13]. The accuracy of depth measurement was influenced significantly by the lateral heat flow and the contact resistance. The results showed that the developed method enables an accurate depth determination over a wide range of thicknesses and blind borehole diameters in CFRP samples. A new approach for the automatic detection and classification of defects in composite materials for aeronautics was developed and tested [21]. It approximates the temperature decay, induced by a short heat pulse, with an exponential model made of three parameters. These parameters were able to describe the behavior of the specimen, separating homogeneous regions from defective ones and categorizing the latter depending on their depths.

Testing of specially designed and fabricated coupons under uniaxial tension and three-point bending were conducted in this study while monitoring with acoustic emission and digital image correlation. These tests were selected to enable investigation of a wide array of defect configurations in a suitable time frame. Acoustic emission was employed in both tests to detect and evaluate the effect of induced defects on the mechanical properties, and DIC was used to monitor damage progression in bending specimens.

The effect of manufacturing defects on structural performance and failure of composite laminates has not been fully investigated, especially for those defects with small geometrical features. This investigation seeks to provide an improved understanding of the influence of defects that are sometimes discovered during the manufacturing process with respect to integrity of the part or component. The innovation lies in using advanced methods to capture the effect of defects through the detection and evaluation of stress waves in small scale carbon fiber reinforced specimens which include AFP defects. This method can be used to determine if these defects warrant immediate repair to ensure part integrity and may eventually lead to a reasoned and experimentally validated approach to acceptance/rejection of components unintentionally manufactured with AFP defects.

2. Experimental work

Tensile and three-point bending specimens were designed, manufactured, and subsequently tested at the University of South Carolina, McNair Center for Aerospace Innovation and Research. Commonly encountered manufacturing defects were intentionally placed in all specimens, with the exception of specimens used as controls (hereafter referred to as ‘pristine’ specimens).

2.1. Specimen geometry

2.1.1. Tensile coupons

Two main considerations were used to design the tensile specimens; a) laminate stacking sequences were intended to approximate thin shell structures, akin to fuselage skin components, since these types of laminates are most likely to be fabricated using the fiber placement process, and b) the small number of laminae served to accentuate the effect of a defect in a single layer. The laminate was further constrained to be near quasi-isotropic in response yet still possessing some degree of orthotropy to investigate alternate orientations of the inserted defects. With these thoughts in mind, two representative layups consisting of seven plies were selected and are referred to by the orientation angle of the center ply (which contains the defect), namely “Zero” and “Ninety”. Layups are shown in Table 1. Note that each laminate possesses different stiffness characteristics due to the orientation angle composition of each stacking sequence. The Ninety configuration contains two axial (0°) plies as opposed to only one in the Zero configuration and thus generates a larger axial stiffness. Pristine specimens for each directional configuration were utilized for comparison to the specimens having defects.

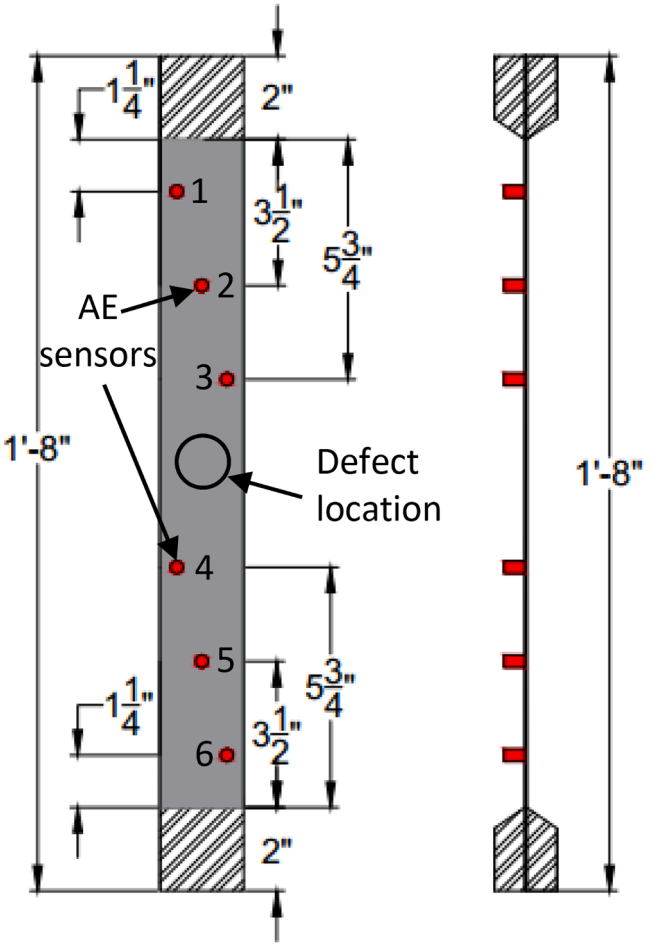

Fig. 1. Tensile Specimen Geometry and AE Sensor Layout.

The geometry of the tensile specimen is shown in Fig. 1. The thickness of each specimen, based on a ply thickness of 0.0055″ (0.140 mm), was 0.0385″ (0.9779 mm). The non-standard planar dimensions were implemented for two reasons: to provide more room for an inserted defect, located at the center of the specimen as denoted by the black circle (Fig. 1); and to generate improved results for the AE technique used during testing.

2.1.2. Three-point bend (3 PB) with doubler specimens

A sketch of the specimen is provided in Fig. 2. The specimens were nominally twelve inches long and two inches wide with a four-inch long centrally-located doubler, which was composed of fabric material and was intended to approximate an attachment area for a stiffener. Under three-point bending, cracks tended to form at the interface between the skin and the end of the doubler. These cracks subsequently led to progressive damage within the skin layer adjacent to the doubler and also

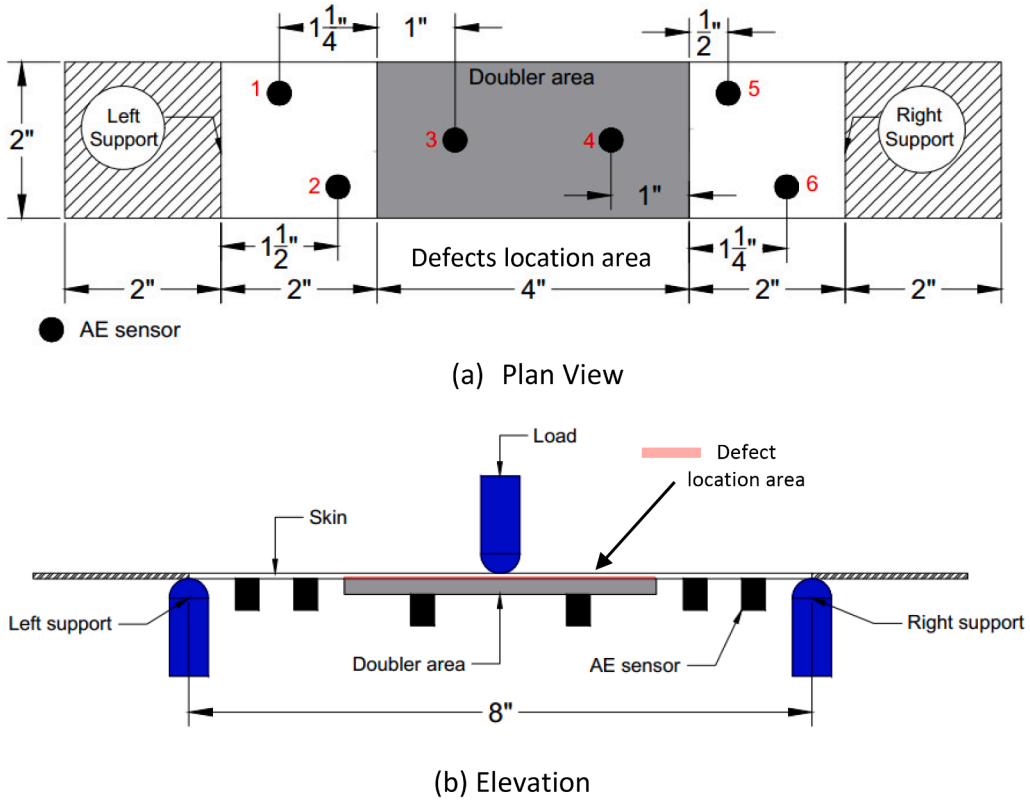

Fig. 2. Three-Point Bend Specimen Geometry.

Table 2
Layups for Three Point Bending Test Specimens.

Skin layup			Doubler layup		
Ply	Type	Orientations	Ply	Type	Orientations
1	IM7/Tape	45	1	8552/SGP196P Fabric	45
2	IM7/Tape	−45	2	8552/SGP196P Fabric	−45
3	IM7/Tape	0	3	8552/SGP196P Fabric	0
4	IM7/Tape	90	4	8552/SGP196P Fabric	45
5	IM7/Tape	45	5	8552/SGP196P Fabric	45
6	IM7/Tape	−45	6	8552/SGP196P Fabric	0
7	IM7/Tape	−45	7	8552/SGP196P Fabric	−45
8	IM7/Tape	45	8	8552/SGP196P Fabric	45
9	IM7/Tape	90	9	8552/SGP196P Fabric	45
10	IM7/Tape	0	10	8552/SGP196P Fabric	−45
11	IM7/Tape	−45	11	8552/SGP196P Fabric	0
12	IM7/Tape	45	12	8552/SGP196P Fabric	45

often delved into lower plies within the skin. As opposed to the tensile specimens discussed earlier, this scenario provided two advantageous features to investigate the effect of defects; a) the location of damage was known, and b) the progression was slower and easier to track experimentally.

The specimens and doublers were composed of 12 plies each having the orientations listed in Table 2. The bending specimens have AFP defects embedded in the 45° skin ply directly underneath the edge of the doubler. This results in a shorter distance available to insert the defect, which motivated the wider two-inch dimension. The locations of defects are discussed in the next section. Initial tests used a single inserted defect, however often the crack did not form on the side of the intended damage. Therefore, subsequent tests (discussed in this study) inserted a defect at each end of the doubler to better understand and highlight the effect of the defect.

2.2. Defect configuration

The defect types considered here are a subset of possible AFP defects observed during the fabrication process and are listed in Table 3 along with their icon representation. Several defect types emerged as unique configurations that serve as the building blocks for this research, namely gaps, overlaps, twisted tows, and wrinkling. Icons representing their idealized geometry are shown in Table 3 marked with shading representing the thickness build up regions.

Table 3
Defect Classification and Building Block Configurations (shaded) [After [19]].

Gap	Overlap	Folded Tow
Twisted Tow	Pucker	Wrinkling
Bridging	Missing Tow	Splice
Loose Tow	Position Error	FOD

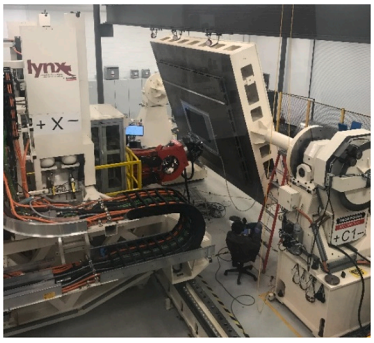

(a) AFP Machine

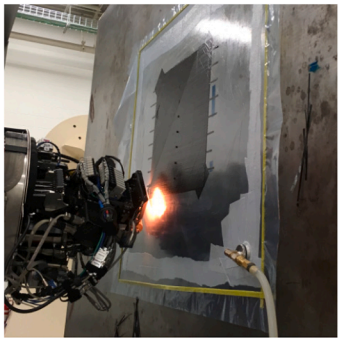

(b) Close View of the Panel

(c) Curing by Autoclave

(d) Water Jet Cutting Apparatus

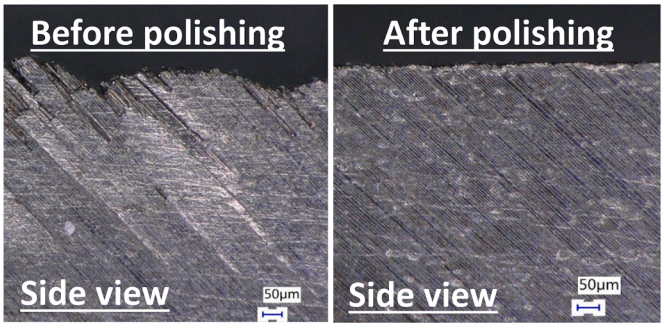

(e) Polishing

(f) Fiberglass Tabbing

Fig. 3. Tensile Coupon Manufacturing Processes.

2.3. Design and fabrication of tensile coupons

The AFP Lynx machine and autoclave at the McNAIR Center at the University of South Carolina (Fig. 3) were used to manufacture the panels using ¼ inch tows of Hexcel IM7-8552 material. Multiple tensile coupons were generated together as part of a single panel for each defect, with the coupon specimens being machined after cure using a water jet cutting apparatus (Fig. 3-c and 3-d). All plies were fiber placed with some defects being intentionally programmed into the part (gaps and overlaps) while the others were inserted by hand (twists and wrinkles). Pristine specimens for both the Ninety and Zero configurations were fabricated as separate panels. After cutting, polishing and tabbing were completed (Fig. 3-e and 3-f). Three specimens representing each defect type were tested. Specimens were named as "Defect.Configuration.Specimen Number" as shown in Table 4 (i.e. P.0.1 refers to pristine, zero configuration, specimen number one).

2.3.1. Gaps and Overlaps:

The development of gaps and overlaps during the AFP fabrication process is attributable to several different mechanisms, including misalignment of courses, unintended movement of tows during lay-down, and inherent mismatches between courses that arise from

Table 4
Tensile Specimen Naming Convention.

Zero configuration		Ninety configuration	
Defect.Configuration. Number	Defect Description	Defect.Configuration. Number	Defect Description
P.0.1, P.0.2, P.0.3	Pristine	P.90.1, P.90.2, P.90.3	Pristine
G.0.1, G.0.2, G.0.3	Gap	G.90.1, G.90.2, G.90.3	Gap
O.0.1, O.0.2, O.0.3	Overlap	O.90.1, O.90.2, O.90.3	Overlap
T.0.1, T.0.2, T.0.3	Twist	N/A	N/A
W.0.1, W.0.2, W.0.3	Wrinkle	N/A	N/A

complex surfaces or curvilinear path definitions. Several types of (secondary) defects illustrated in Table 3 can also be considered as combinations of neighboring gaps and overlaps (for example, folds or missing tows), therefore investigation of gaps and overlaps was warranted as a basic building block for AFP defects.

Gaps and overlaps were inserted into the defect layers across the entire width (for Ninety configuration) or length (Zero configuration) of the tensile specimens. These defects were directly programmable within the AFP software environment to ensure accurate and consistent placement of the defects. The programs dictated neighboring courses to leave a ½-tow gap or overlap between courses (each course contains eight tows), demonstrated by the cartoons in Fig. 4. Successive plies were laid over these defects in the middle layer, and during cure regions of resin-rich areas (for gaps) and thickness build-up (for overlaps) were observed. The size of gaps and overlaps was checked at the edge of the coupons using a microscope as presented in Fig. 5.

2.3.2. Twists

For defects that cannot be inserted automatically, techniques were developed for by-hand insertion into the middle layer of the Zero configuration (the Ninety configuration did not provide enough length for useful insertion of such defects). Insertion of twists was completed by removing the center tow for a coupon and then re-inserting by hand, with one half-twist introduced into the middle tow of the Zero configuration. Care was taken to maintain consistency with respect to length for each twist. Because it is difficult through visual inspection at the edges in a similar way as gaps and overlaps to detect a twist embedded in the middle of the coupon and to fully capture these defects, multiple cutting planes (cut 1 through 4) are needed at different cross-sections (Fig. 6).

A four-inch-long twist was hand-placed in the panel and the resulting coupon was cut along the multiple planes as described in Fig. 6. For each cut, the specimen was polished to obtain a smooth surface. The resulting images captured using the digital microscope are shown in Fig. 7 for cutting plane 1 through 4 respectively. The progression of the twist formation is depicted starting with cut 1 where a small resin rich area is observed next to a fold both having a size of around 200 μm. The size of tow folded over itself as well as the size of the resin rich area increases from cut 1 through 4. Cut 4 corresponds to the mid-section of the twist which is characterized by an increase in the thickness of the layer since the tow is fully folded over itself and two resin rich areas from each side.

2.3.3. Wrinkle

A circular tool was used to provide a consistent template for the amount of inserted material. As shown in Fig. 8, specific tows were removed after AFP laydown of the middle ply, and then re-inserted by hand with the intentional defect at the proper location (the extended tows visible on the tool are the specific tows that were replaced). Results of the insertion are shown to the right in Fig. 8 before laydown of the successive ply, which tends to fold the wrinkle upon itself. Micrographs of the resulting cross-sections are shown in Fig. 9.

2.4. Design and fabrication of three-point bending specimens

Regarding the three-point bend specimen, a special tool with a 4-inch wide groove was required to accommodate for the variable thickness of the specimens. The fabric layers were cut using an automatic GERBER cutter machine and hand placed on the tool in the designated space for the doubler. The fabrication of the skin panel was accomplished using

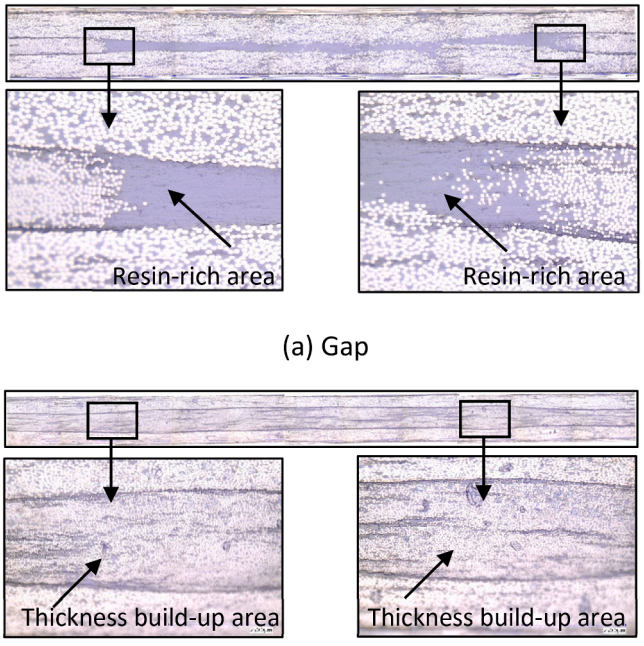

Fig. 5. Insertion of Gap and Overlap into Center Ply (Images Taken by the Authors).

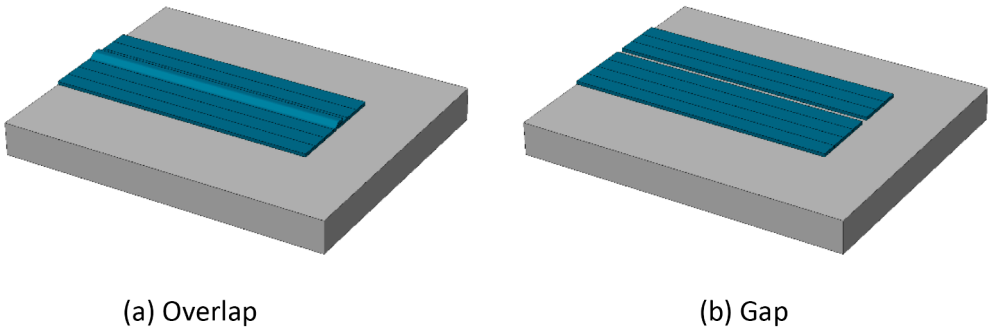

Fig. 4. Idealized Programmed Patterns for Gaps and Overlaps.

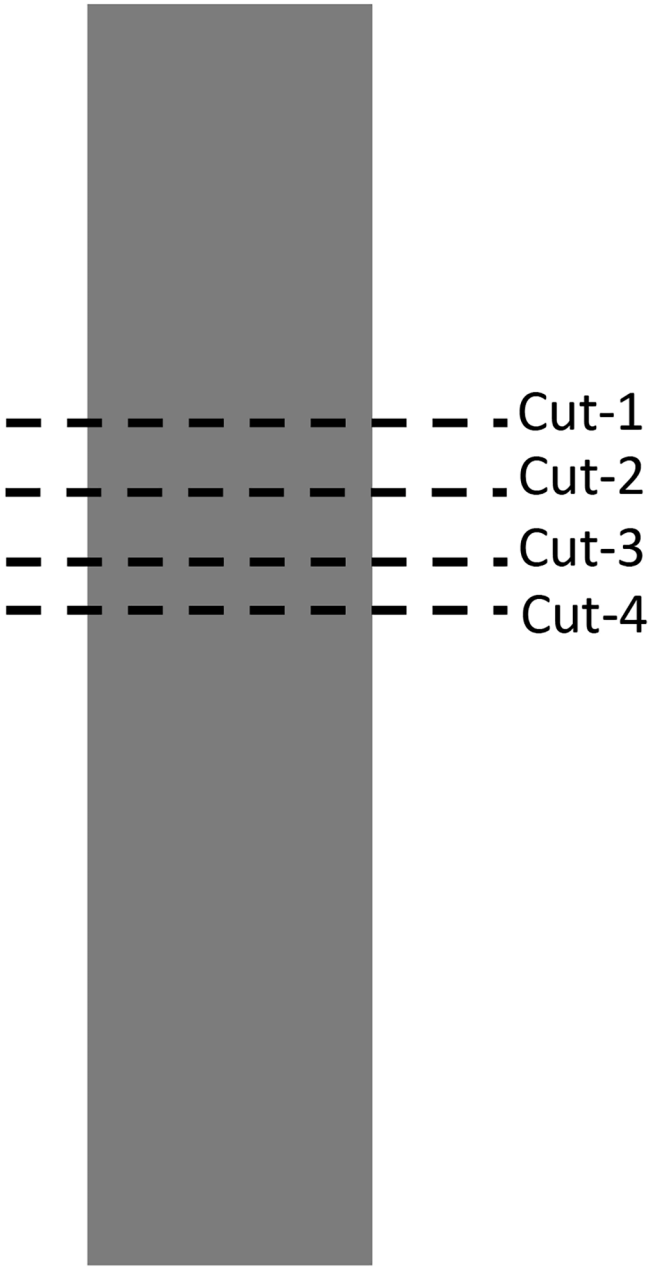

Fig. 6. Cutting planes for the twist defect.

the AFP Lynx machine at the McNAIR Center at the University of South Carolina (Fig. 3) with ¼ inch tows, Hexcel IM7-8552 material. Defects were inserted by hand into the outermost ply of the skin following the blueprint shown in Fig. 10. The skin and doubler were assembled where defects coincide with the layer in contact with the doubler and then co-cured in the autoclave. The specimens were cut according to the profile shown in Fig. 10 and their edges were polished. A total of three coupons of each type: pristine, gap, overlap, twist, and wrinkle are obtained for each layup.

For defect insertion, it is required that the location of the defects be aligned at the edges of the doubler in the last layer of the skin oriented at +45°. In addition, the defect cannot extend beyond the coupon boundaries, so it does not interfere with the neighboring ones. In such a case, manual intervention is required to insert a gap or overlap at the exact location and automatic programming cannot be used to insert such short and discontinuous defects. To facilitate manual operation, a blueprint of Fig. 10 was reproduced on a see-through rigid plastic bag and the locations of the defects were marked on the skin. To replicate a gap manually, the following procedure was used: 1) cut the tow at the boundaries of the coupon, 2) peel the tow from the substrate, 3) slit the tow at the required gap width, and 4) place the remaining of the tow in its original location. To replicate an overlap manually, the following procedure was used: 1) slit a tow with the required gap width, and 2) place the slit tow at the defect location. The same procedure discussed in the previous sections to insert a twist and a wrinkle is followed. The last layer of the skin with all the defects inserted is shown in Fig. 11. Examination of defects after cure shows similar results as the ones presented earlier in Figs. 5, 7 and 9.

2.5. Acoustic emission setup

Six AE broadband sensors, type B-1025 (Digital Wave Corporation, Castle Rock, Colorado), were used having an operating frequency range between 50 and 2000 kHz. Hot melt glue was utilized as a coupling agent to fix the sensors on one surface of the specimens. In-Line low power AE signal preamplifiers (IL-LP, MISTRAS Group Inc., Princeton Junction, New Jersey) supplied 26 dB gain and band pass filters from 100 to 1200 kHz were used. The digital AE data acquisition system was a 24-channel Micro II Express (Mistras Group Inc.). The AE sensor layout for both tensile and three-point bend tests are shown in Figs. 1 and 2, respectively. Photographs of the test setup are shown in Fig. 12. Prior to conducting loading of the specimens, a background noise check was performed to identify the appropriate testing threshold (31 dB). Pencil lead breaks (PLB) were utilized prior to loading to assess the sensitivity of each sensor and to ensure that the coupling was consistent for all sensors.

2.6. Testing procedure

Tests were conducted using a Material Testing System (MTS 810) with a servo-controlled hydraulic loading frame. Tensile specimens were loaded in displacement control at a rate of 0.02 in./min. The first specimen of each type was loaded to failure without attaching AE sensors to determine the ultimate capacity. The results served as a guide for the next part of the test; hence, subsequent specimens were loaded to 80% of the ultimate load. Once 80% of the ultimate load was reached, AE sensors were removed to protect the sensors and the specimen was loaded to failure. For three-point bending specimens, the AE sensors were able to be attached all the way through final failure and used for all tests due to the non-catastrophic failure mode. They were loaded in displacement control at a rate of 0.078 in/min. For both tests, loading was applied until ultimate failure and load–displacement from the loading machine and the AE data acquisition system were synchronized.

3. Analysis results

Nondestructive methods have been developed to detect and evaluate damage growth in materials such as steel [28]; Yu et al., 2011, concrete [3,14], and fiber reinforced polymer composites [11,6,4,35,33,34,30]. These methods include; a) assessment of active damage progression using AE time and frequency domain signal features, b) source localization of AE events, and c) classification of crack progression using pattern recognition. Two methods based on signal strength features are described in this study including temporal evolution of Cumulative Signal Strength (CSS) and Intensity Analysis (IA).

3.1. Tensile specimen results

The average values of stiffness and ultimate strength for Ninety and Zero configurations are summarized in Tables 4 and 5, respectively. As expected, Ninety configuration specimens showed higher stiffness and ultimate strength compared to Zero configuration specimens because they contain two axial (0°) plies versus only one axial ply (Table 1).

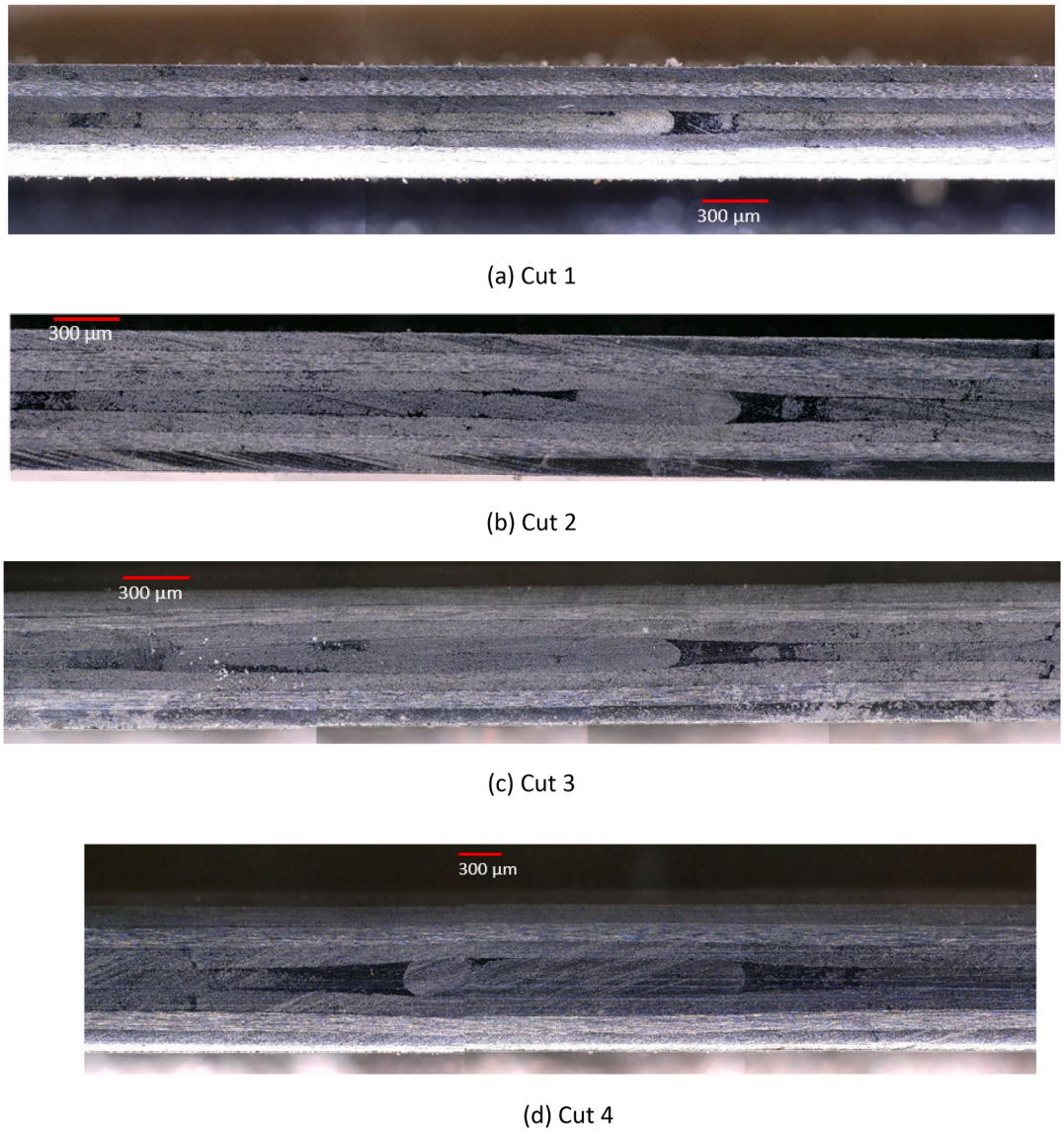

Fig. 7. Microscopic images of a twist at different cross-section at 50X magnification (Image Taken by the Authors).

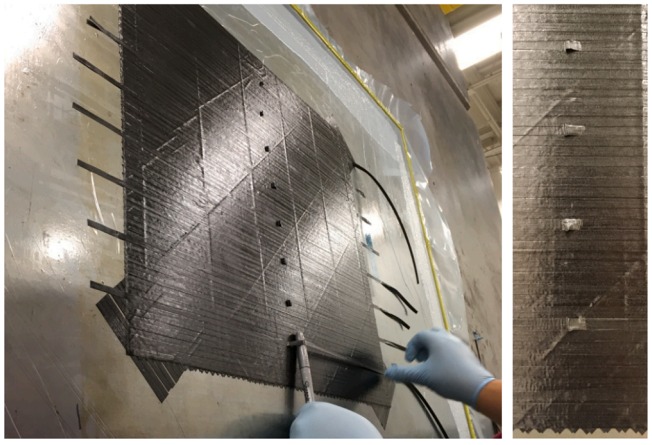

Fig. 8. Insertion of Wrinkles into Center Ply.

Based on each defect configuration, one can assume that the effect of removing material (from the orthogonal gap) or adding material (due to the overlap occurring across the width) for the Ninety configuration is to decrease/increase the stiffness and failure characteristics compared to a pristine specimen. The relatively small differences are likely attributed to the defects being situated in a 90° layer, which already possesses small stiffness in the loading direction and is the likely source of damage initiation due to matrix cracking. Therefore, inserting these defects into the weakest ply of the laminate may not produce large differences from the pristine configuration.

Comparisons of the gaps, wrinkles, and twists in the Zero configuration does not seem consistent with traditional expectations, where one would expect the full-length gap configuration to exhibit lower stiffness and strength parameters compared to the specimens that contain smaller localized defects (even when we compare to the two consistent specimens for wrinkling). The effect of the localized defects was difficult to distinguish from this test. Therefore, further investigation of these defects using a more detailed analysis method (AE is selected in this investigation) for tensile specimens and an informative loading state (three-point bend) should provide greater insight. Moreover, it was

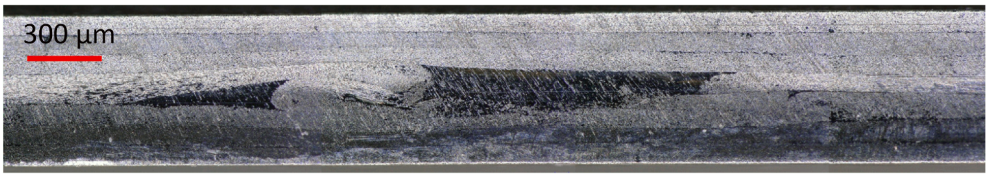

Fig. 9. Micrograph of Wrinkle (Image Taken by the Authors).

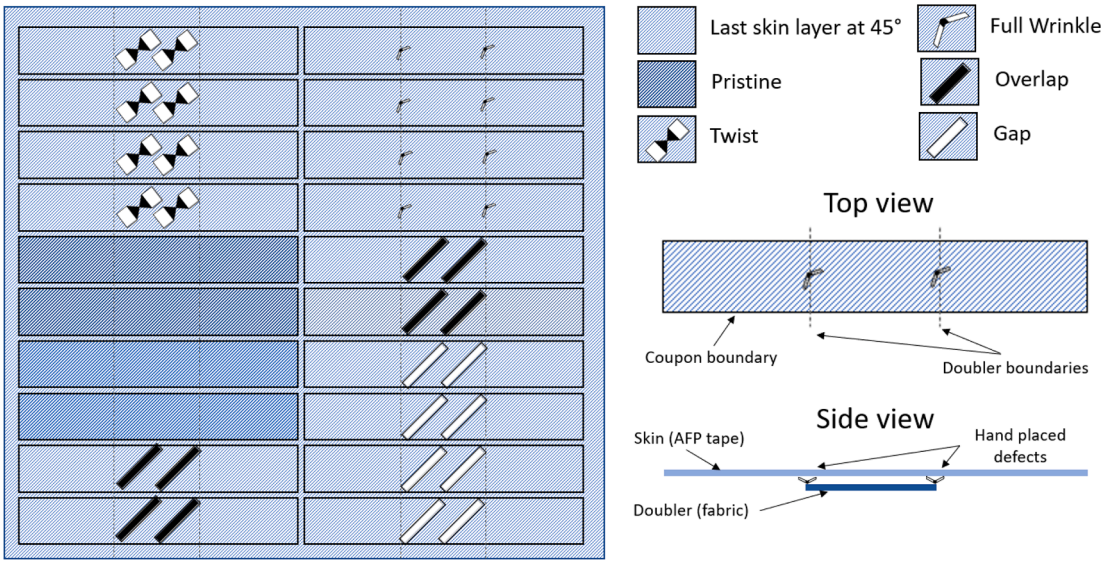

Fig. 10. Double Defect Locations in Three Bend Specimens.

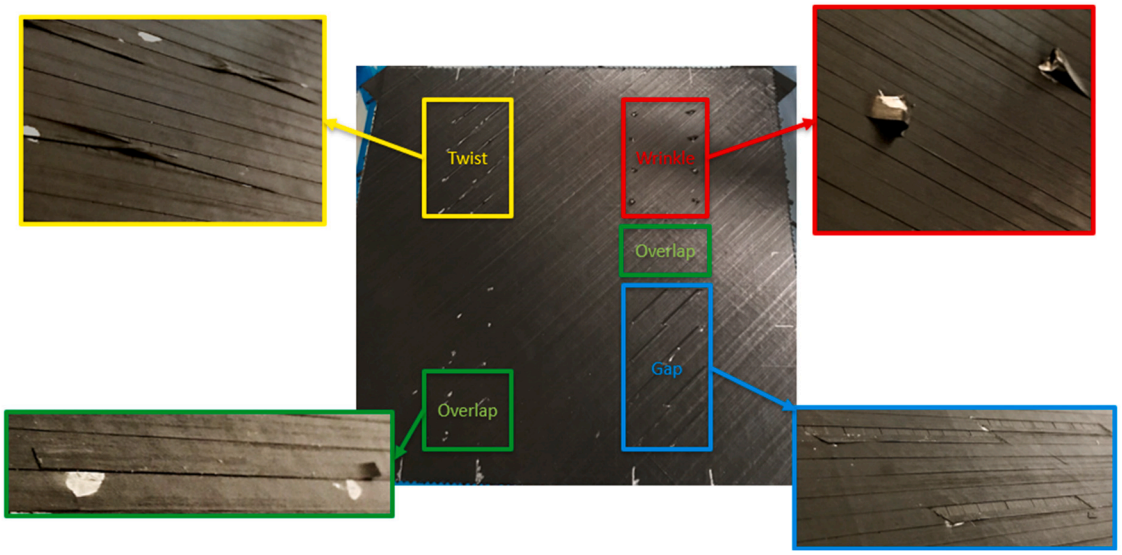

Fig. 11. Defect Placement in the Skin Layer.

observed that these pristine specimens also contained some non-intended defects which may influence observations on the effect of intended defects.

In tensile coupons, the progressive damage starts first in the 90° layers, then + -45° and finally in the 0° where the defects were placed, hence the effect of defects is more delayed. In the bending coupons, the stress state is much more complex; in addition, the defects are placed at the edge of the doubler where higher stress concentration occur, therefore their effect is more noticeable.

3.1.1. Classification of crack growth based on Cumulative signal strength (CSS)

Acoustic emission data was recorded and post-processed using AEwin software [AEwin E4.30, Mistras Group Inc., Princeton Junction, New Jersey]. AE data initiated early in the test (approximately 10% of ultimate) and continued thereafter. Cumulative Signal Strength (CSS) as a function of load of pristine specimens is shown in Fig. 13. This parameter is used to assess the level/type of damage occurring within the specimen and aids in defining failure regions. Significant increases in

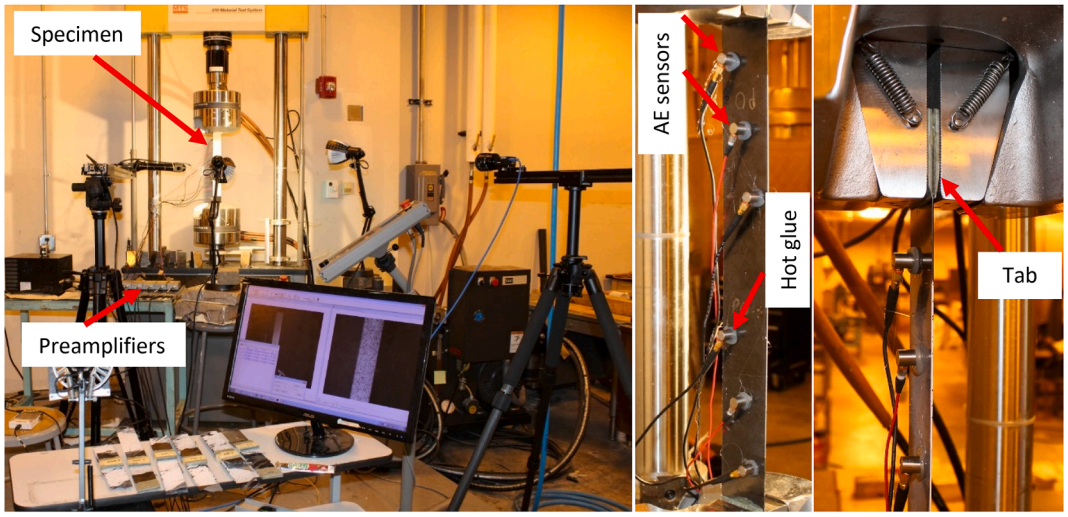

(a) Tensile Specimen

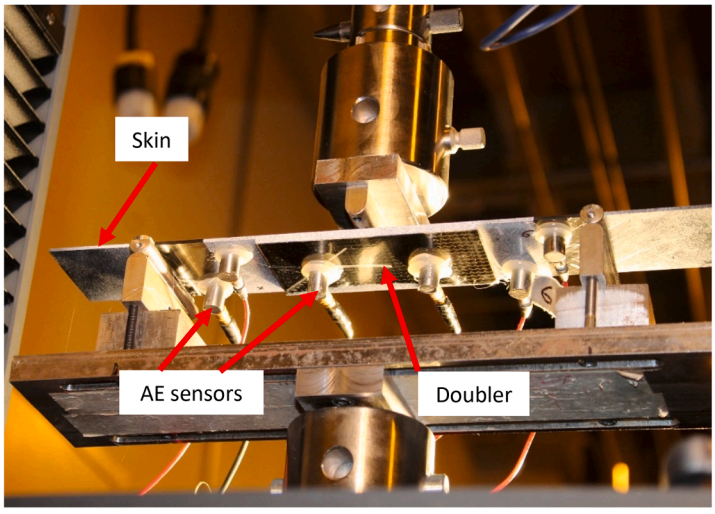

(b) Three-Point Bending Specimen

Fig. 12. Tests Setup of Tensile and Three-Point Bend Specimens (Image taken by author).

Table 5
Average Values for Ninety Configuration Specimens.

Specimen Designation	Stiffness Estimate (msi) /STDEV/COV(%)	Ultimate Failure (ksi)/ STDEV/COV
P90	8.290/0.11/1.32	105/9.41/8.95
G90	8.213/0.08/1.01	106/5.97/5.6
O90	8.453/0.4/4.75	112/5.78/5.14

CSS compared with previous stages were observed and used to inform damage progression as load increased. Different ranges of crack behavior, illuminated by changes in the slope of the cumulative signal strength curve, can be detected for both Ninety and Zero configurations. Cumulative signal strength can be compared between specimens to estimate relative damage and identify the types of damage that each failure region represents. For instance, in a typical tensile test as shown in Fig. 13, the Ninety configuration showed lower damage than the Zero configuration under the same load (higher signal strength indicates more damage accumulation). This is due to the orientation angle composition of each stacking sequence. The Ninety configuration contains two axial (0°) plies as opposed to only one in the Zero configuration and thus generates a larger axial stiffness. Furthermore, cracks initiated and progressed earlier in the Zero than in the Ninety configurations which caused more AE events detected at early loading stage of the Zero configuration. This confirmed the stiffness and strength behavior previously explained. Fig. 13-b shows an example of defined failure regions using CSS. These regions were identified based on the shape of CSS curve. The first region R1 (in Fig. 13-b)) is the linear undamaged region (where the effective stiffness is most accurately calculated) which transitions to the second region, R2, when acoustic events indicate matrix cracking is occurring. The third region, R3, with higher incidence of events and signal strength, indicates damage growth and progression. Lastly, another significant jump, R4, can indicate major damage events such as fiber breakage leading to ultimate failure.

While clear difference of damage growth was seen between the pristine specimens of the two configurations (Fig. 13a), this was not the case when comparing each defect with pristine specimen of the same configuration. Figs. 14 and 15 show CSS versus load relations of Zero and Ninety configurations. Up to 3,000 lbs. of loading, CSS curves of the defect and pristine specimens were mixed together, and it was difficult to observe the effect of the localized defects. Applying more load (i.e. more than 3,000 lbs.) caused more damage which affected the convergence of the CSS curves. Therefore, in-depth analysis should be

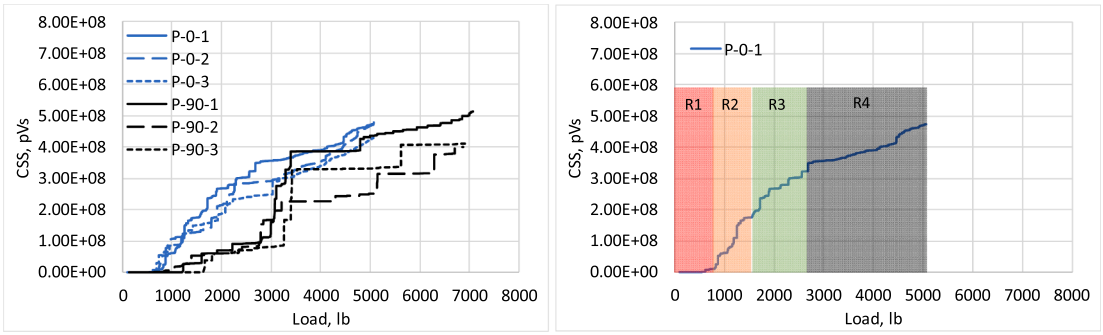

(a) Zero and Ninety Configurations (b) Example of Failure Regions

Fig. 13. Cumulative Signal Strength (CSS) Versus Load of Pristine Specimens.

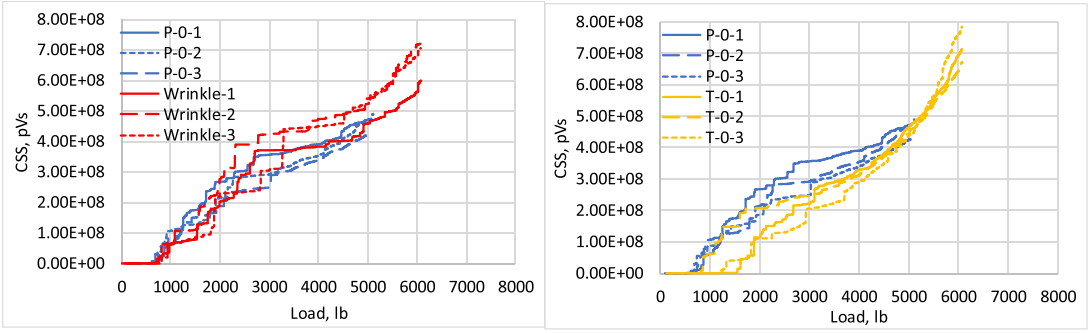

(a) Wrinkle and Pristine (b) Twist and Pristine

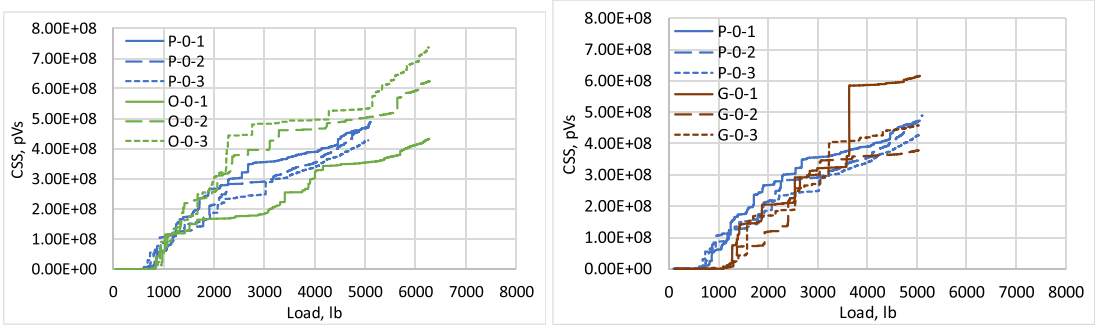

(c) Overlap and Pristine (d) Gap and Pristine

Fig. 14. CSS Versus Load of Zero Configuration Specimens.

conducted to investigate the effect of defects on the behavior of tensile coupons (i.e. the change in the slope of CSS curve compared with the previous step may detect the effect of defects) as discussed in the next section.

3.1.2. Damage quantification using Intensity analysis (IA)

Intensity Analysis is a method first developed to categorize damage based on AE data in composite pressure vessels [15]. Two parameters are calculated based on signal strength including historic index and severity. Historic Index, H(t), given by function 5–1, is sensitive to the change in slope of the CSS curve with respect to time using a historical approach (ratio of the CSS of recent hits to the CSS from all hits). Severity, Sr, is the average of the 50 events having the highest signal strength given by function 5–2 [17]. The damage level of a structural element can be approximately assessed by tracking the changes over time of these two parameters. The intensity analysis chart of AE activity is created by plotting the maximum Historic Index (HI) versus the severity values. When events are located toward the top right corner of the intensity analysis chart, they are generally related to increased damage [17,14,2]. Formulas 5-1 and 5-2 for HI and severity are provided below:

$$H(t) = \frac{N}{N\text{-}K} \frac{\sum_{i=K+1}^{N} S_{ti}}{\sum_{i=1}^{N} S_{ti}} \tag{5-1}$$

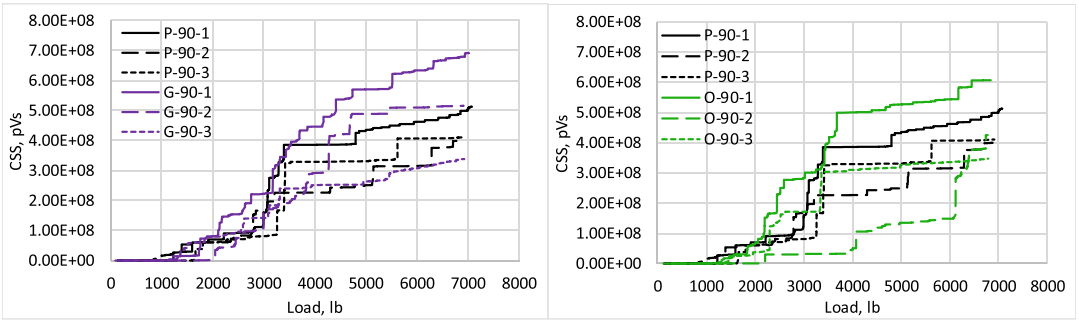

Fig. 15. CSS Versus Load of Ninety Configuration Specimens.

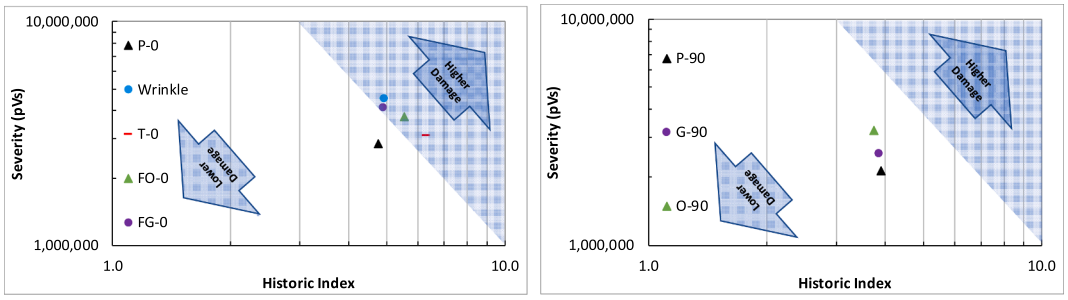

Fig. 16. Intensity Analysis Condition Assessment Charts of Tensile Specimens.

$$S_r = \frac{1}{50}\sum_{i=1}^{i=50} S_t \qquad (5.2)$$

where N = number of hits up to a specific time (t); S_{ti} = signal strength of the ith event; and K = an empirically derived constant that varies with the number of hits. One value for K that has sometimes been suggested in the literature is [14,23]: (1) not applicable if $N \leq 50$; (2) $N - 30$ if $51 \leq N \leq 200$; (3) 0.85 N if $201 \leq N \leq 500$; and (4) $N - 75$ if $N \geq 501$.

Intensity analysis was applied to evaluate the level of potential damage (i.e. matrix cracking, and delamination) occurring in the pristine and defect specimens under tensile loading. Fig. 16 shows the intensity analysis charts of tensile specimens. Each point in the figure represents the average value of three specimens. In Fig. 16a the high historic index and severity values approach the upper right corner of the charts indicating the most damage in defect specimens with Zero configuration compared to the pristine. In Ninety configuration, the difference between the defect and pristine specimens was not clear as the defect specimens have higher severity and lower historic indices compared to the pristine one. The reason is unclear, and it is noted that most of the pristine specimens have unintended defects. Moreover, the size of the defect may not have significant effect in Ninety configuration with higher stiffness compared to the Zero configuration with lower stiffness. Furthermore, the Zero configuration has higher historic index and severity values than Ninety configuration under the same load. This is attributed to AE activity with higher signal strength generated by crack initiation and growth in the Zero when compared to the Ninety configuration.

3.2. Three-point bending (3 PB) test results

Comparison of the pristine versus intentionally embedded defect configurations under three-point bending (3 PB) provided more consistent results concerning the effect of defects. The load–displacement and AE data were continuously recorded for the 3 PB configurations for each defect type (defects on both sides). Three specimens from each group of double defect configuration were tested. Table 6 indicates the relative load levels and stiffness for each specimen, and Fig. 17 shows load–displacement comparison curves between the defect and pristine specimens. There is no clear difference in stiffness between the defect and pristine specimens, however, the initial crack formation load and the ultimate delamination failure load showed a slight effect of defects (Table 7). The load displacement data did not reveal a pronounced effect of the defects. Therefore, further investigation of these defects employing acoustic emission was pursued and results are discussed in the next section.

Table 6
Average Values for Zero Configuration Specimens.

Specimen Designation	Stiffness Estimate (msi)/ STDEV/COV	Ultimate Failure (ksi)/ STDEV/COV
P0	5.989/0.13/2.2	79.82/3.2/4.01
G0	6.137/0.1/1.68	86.34/3.52/4.08
O0	5.976/0.32/5.34	81.24/3.9/4.8
W0 – 3 specimens	5.824/0.44/7.64	85.36/7.71/9.04
W0 – 2 specimens (outlier removed)	6.080/0.07/1.24	89.82/0.5/0.55
T0	6.587/0.06/0.97	93.17/1.89/2.03

All specimens from each group had similar response curves (Fig. 17), with the initial matrix cracking leading to delamination. After the initial load drop, delamination also occurred on the side of the doubler which led to final separation and overall failure (Highlighted failure zone in Fig. 17).

The gap configuration curves (Fig. 17a) predominately mirror the

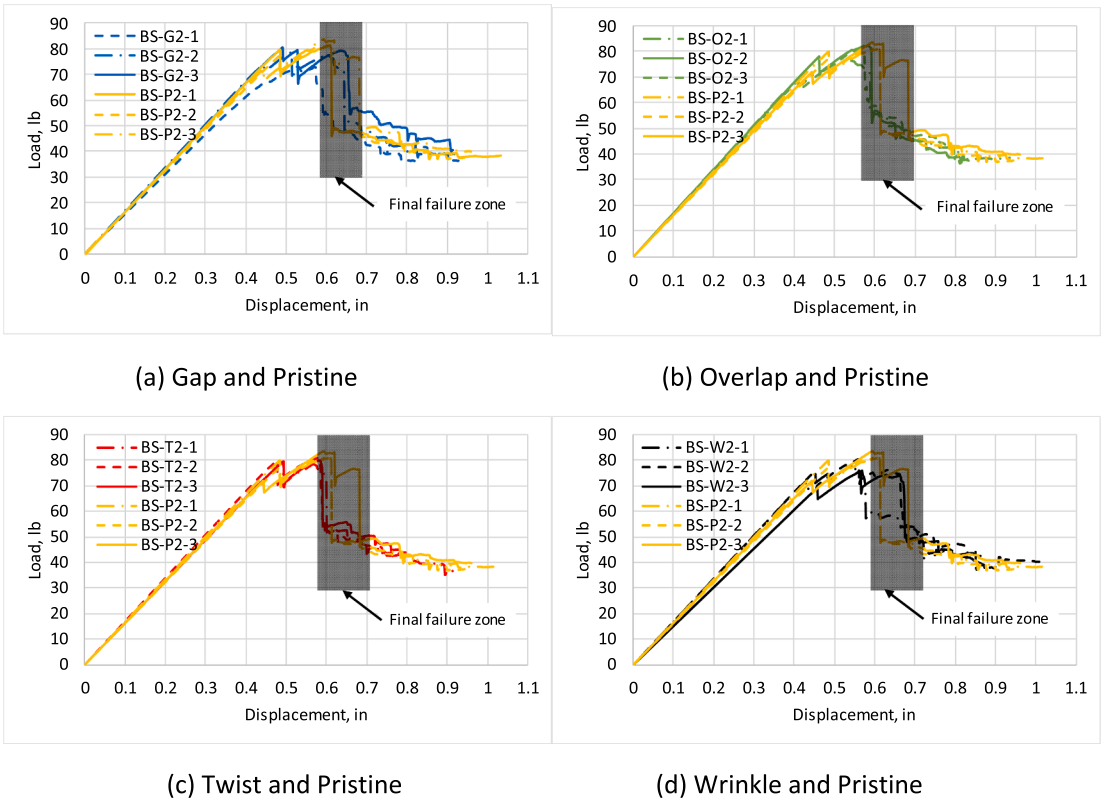

Fig. 17. Load-Displacement for of Three-Point Bending Specimens.

Table 7
Results Summary for 3 PB Specimens.

Specimen Designation	Stiffness (lbf/in)	Initial Crack Formation (lbf), (first load drop, Fig. 17)	Ultimate Delamination Failure (lbf), (last load drop, Fig. 17)
*BS-P2-1,2,3	148.4	71.6	77.0
*BS-G2-1,2,3	149.8	71.4	72.6
*BS-O2-1,2,3	149.4	66.8	74.5
*BS-T2-1,2,3	148.8	74.4	74.9
*BS-W2-1,2,3	150.7	67.9	73.6

*Average value of three specimens.

pristine results with the initial matrix cracking side leading to initial delamination there, though the second peak after delamination tends to be not as pronounced for the gap specimens. In general, not much effect of the gap defect is observed.

The overlap configuration curves on the right (Fig. 17b) dispute the expected notion (adding material provides greater resistance to damage), where two of the three double defect specimens have initial delamination much lower than their baseline pristine specimens. Therefore, more tests are required with different geometry sizes of defects to further investigate this effect. On the other hand, AE data analysis detected the effect of defects clearly as discussed in the next section.

While the responses of twist configuration (Fig. 17c) do not deviate far from the pristine baseline, it was observed that the second ultimate failure peak often does not exceed the initial peak value. More tests and additional techniques should be employed to detect and explain this effect. Lastly, with wrinkle defects (Fig. 17d) one would suppose that it would most closely resemble the overlap configuration (added material near the failure point), though the effect does not seem as prominent.

Fig. 18 shows photographs taken at failure load. Some of the specimens had the first crack (double-skin delamination) initiated at one side, then the second crack initiation and progression occurred at the other side (Fig. 18a). While for other specimens, crack initiation and progression happened at only one side (Fig. 18b).

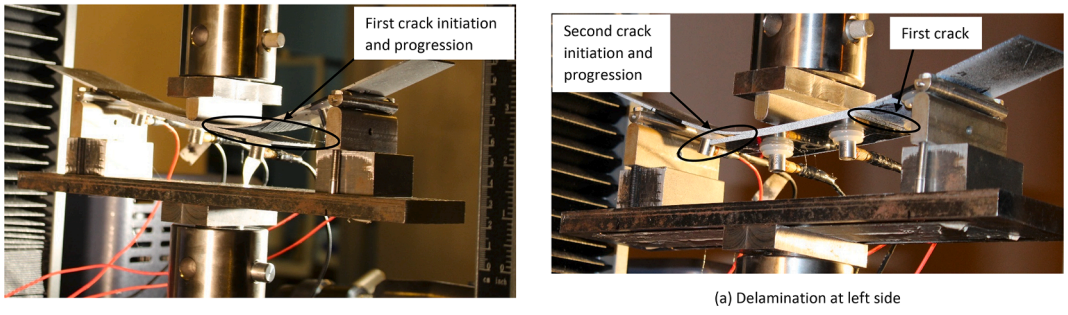

Fig. 18. Photographs taken at failure load (Image taken by author).

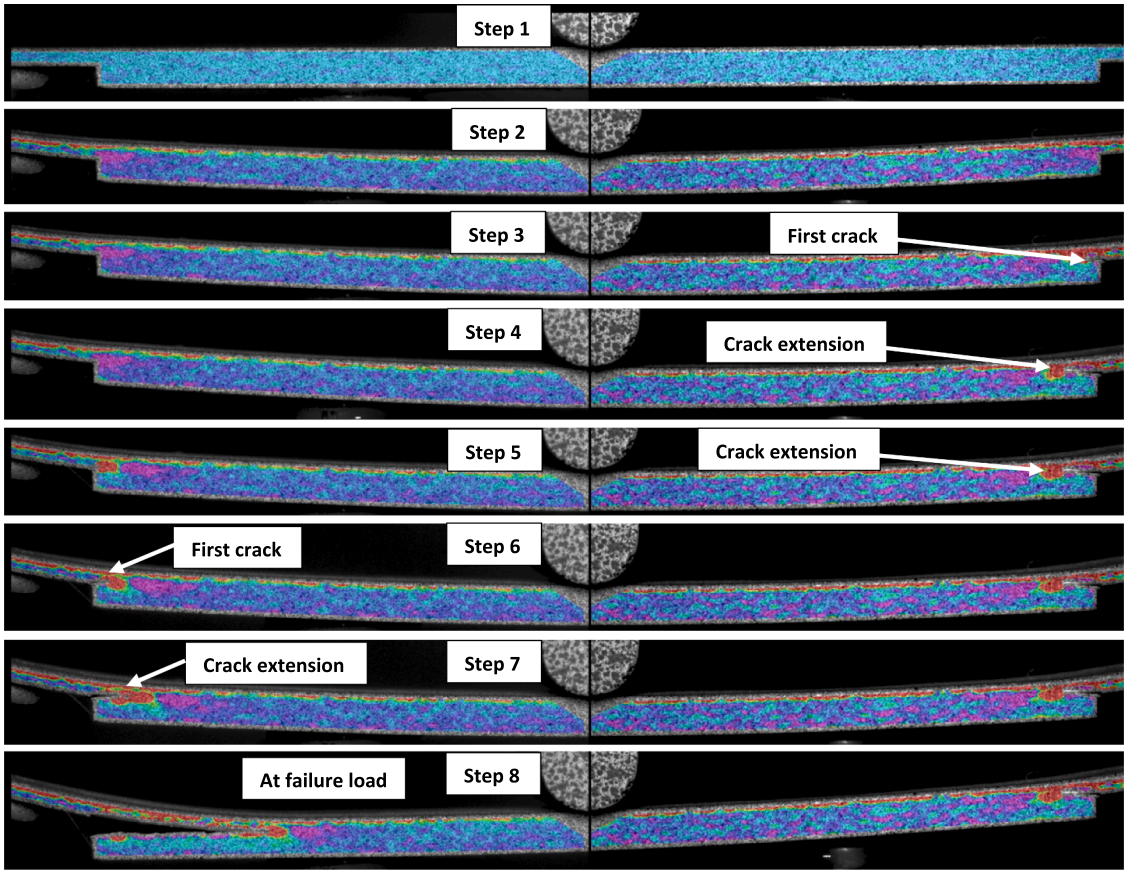

Fig. 19. Example of DIC contours (strain in vertical direction) for 3 PB test of BS-G2-2 specimen (Gap Specimen).

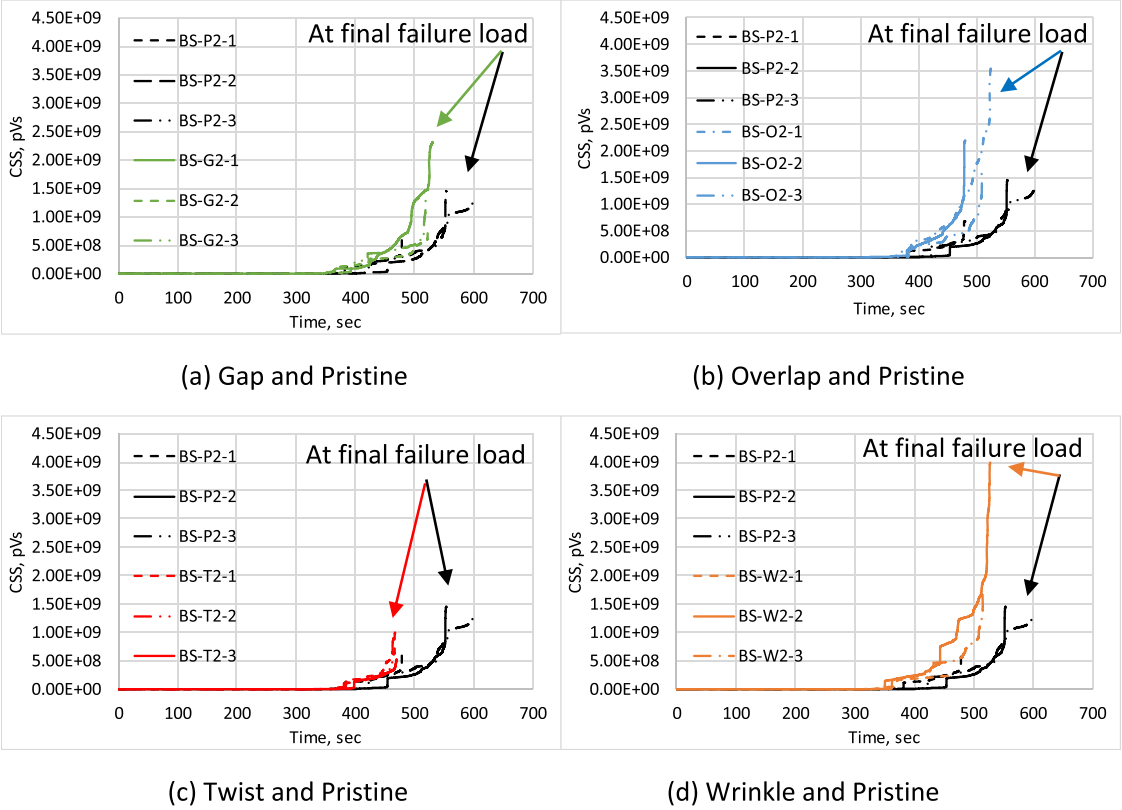

Fig. 20. CSS Versus Time of Three-Point Bending Specimens.

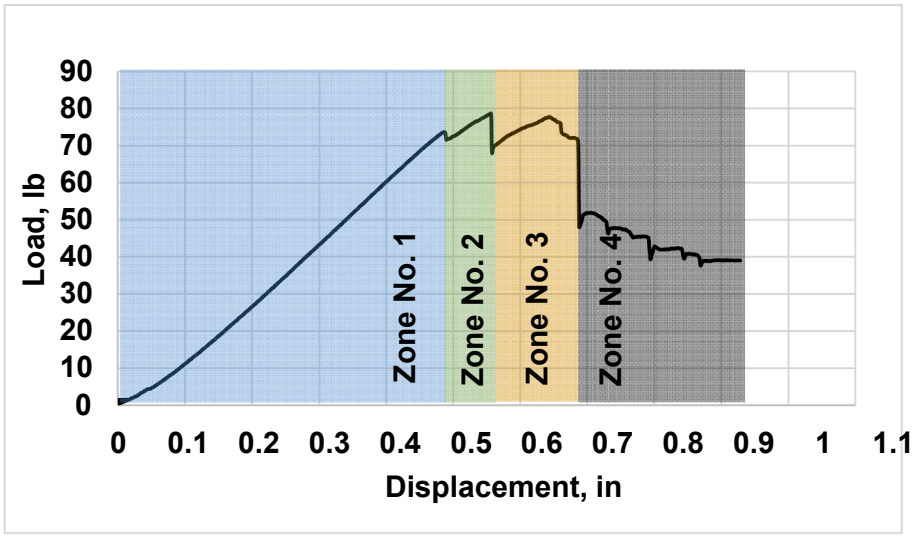

(a) Load-Displacement

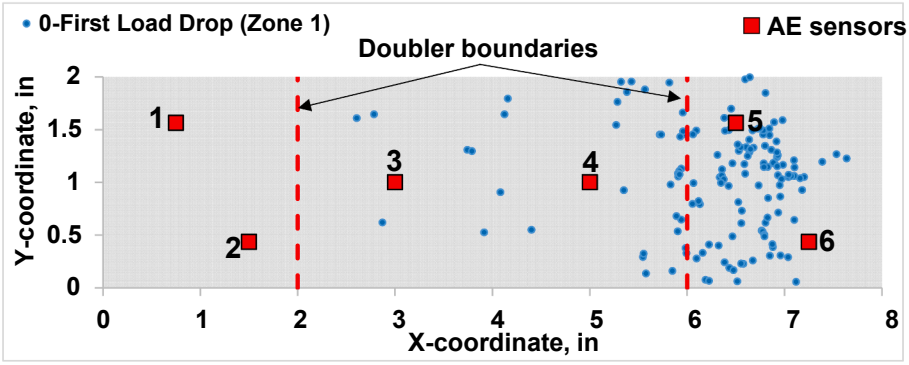

(b) AE events detected during zone 1

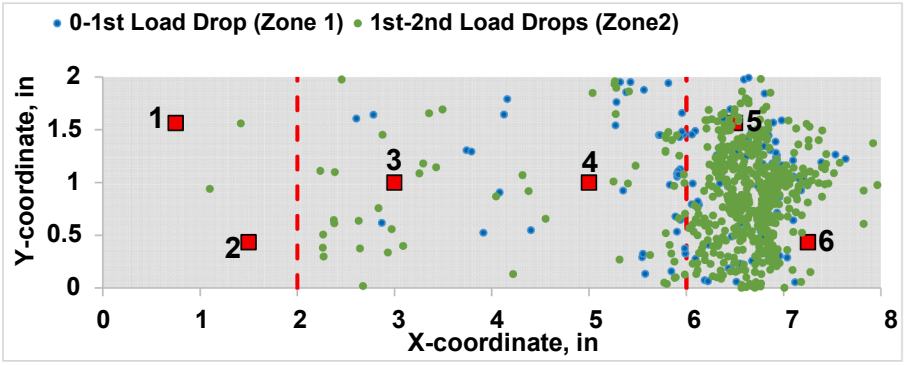

(c) AE events detected during zones 1 and 2

Fig. 21. AE source location for BS-G2-2 specimen during bending test.

3.2.1. Digital Image correlation (DIC) visualization

Failure developments were monitored during the 3 PB test using digital image correlation (DIC). This technique allowed excellent capture and visualization of the front and back edges of the doubler specimens. An example of a typical strain contour obtained from DIC analysis for a BS-G2-2 specimen (Bending specimen with gap defect at both sides of the doubler boundaries, see Fig. 10) is displayed in Fig. 19. The contours denote the level of strain in the vertical direction, which was chosen as the best representation of the relative deformation around the crack tips. As the cracks began to develop and progress (Steps 3–7 in Fig. 19), the evolution of the cracks at the edges was easily detected and tracked even to the naked eye. Step 8 shows the captured delamination at the failure load. These images helped to verify the location of the damage events (extracted from the AE data, explained in the next section) and to provide a measure of the crack growth with respect to the load level. Visualization of each test using the DIC technique synchronized with the load–displacement curve and AE source location plots (explained in the next section) provided an excellent tool for monitoring

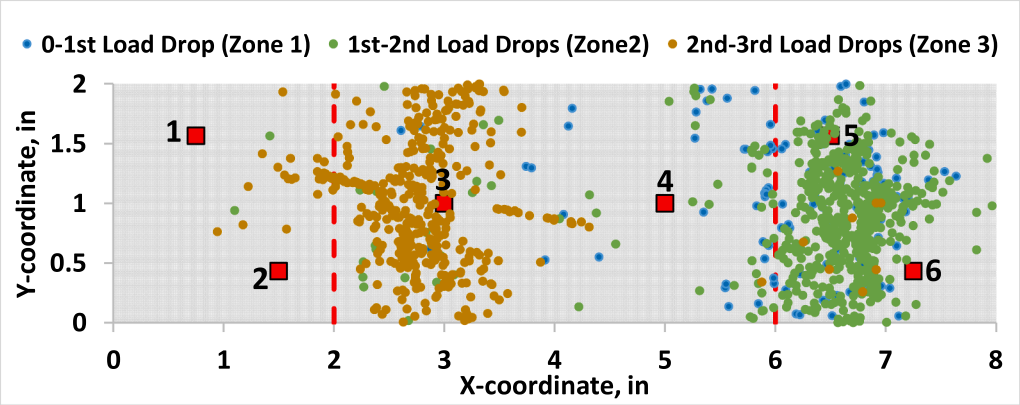

(d) AE events detected during zones 1, 2 and 3

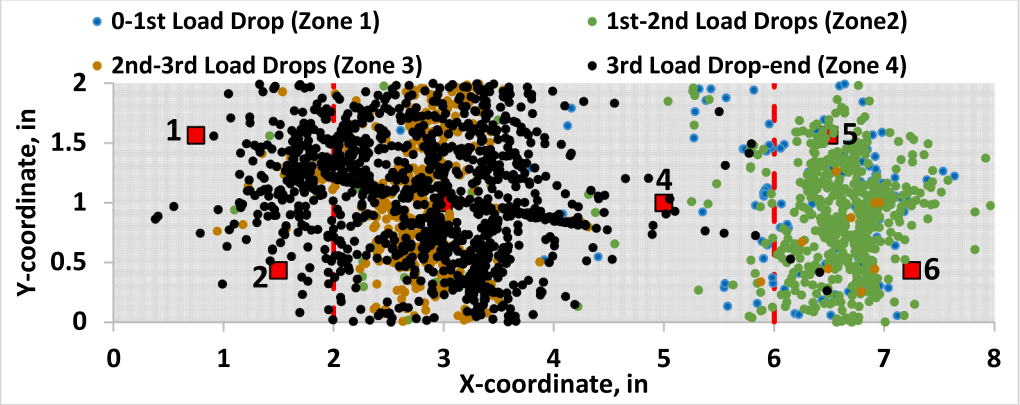

(d) AE events detected during zones 1, 2, 3 and 4 (Complete bending test)

Fig. 21. (*continued*).

the progress and relative response of the 3 PB specimens.

3.2.2. Classification of crack growth based on cumulative signal strength

Cumulative signal strength (CSS) curves of pristine and defect specimens are shown in Fig. 20. As explained in the tensile specimen section, this parameter aids in evaluation of the level/type of damage that is occurring within the specimen and in defining failure regions. Several significant jumps in CSS compared with the previous stages were observed and used to inform damage progression as load increased. Different ranges of crack behavior, illuminated by changes in the slope of the cumulative signal strength curve, can be detected for both pristine and defect configurations. To estimate relative damage and also identify the types of damage, CSS curves of both configurations are compared as shown in Fig. 20. For instance, earlier damage indicated by higher CSS was introduced by each defect group compared with the pristine group. In other words, the Pristine configuration showed lower damage than the defect configuration under the same load (higher signal strength indicates more damage accumulation). All curves in Fig. 20 were plotted up to ultimate failure load as shown in the highlighted regions in Fig. 17.

3.2.3. Source localization of acoustic emission events

Source triangulation algorithms were used based on the time of flight [1]. Wave speeds were determined through 0.3-mm-diameter pencil lead breaks conducted at different locations within the sensor grids [5]. Background noise testing was collected prior to the actual load tests to establish an appropriate test threshold of 31 dB. Fig. 21 shows an example of AE events detected during the bending test of BS-G2-2 specimen. First, load–displacement response, shown in Fig. 21a, was divided into four zones based on the load drops record. Then, source localization algorithm was applied to represent the AE events in 2D plots based on the time frame of each zone as illustrated in Fig. 21b-e. From the beginning of the test to the first load drop (zone 1), most of AE events were located at the right side of the specimen (Fig. 21b) where the first crack happened (step 3 in Fig. 19). During zone 2, as crack extension occurred from the right side towards the mid of the specimen (steps 4 and 5 in Fig. 19), more AE events were detected as described in Fig. 21c. For the period of zones 3 and 4, the second crack was initiated and progressed at the left side of the specimen (steps 6–8 in Fig. 19). This caused substantial amount of AE events collected at the left side as shown in Fig. 21d, e. It can be concluded that AE source localization results agreed with the vertical strain contour described by DIC technique and load–displacement response. Also, it can be used to describe failure developments of bending specimens.

4. Conclusions

This study discusses potential approaches for the evaluation of defects that may occur during the automated fiber placement (AFP) process. Tension and three-point bending tests were conducted on pristine and defect induced specimens. Acoustic emission (AE) as a nondestructive evaluation technique was utilized to investigate correlations between mechanical properties and damage propagation during both tests. The results of the acoustic emission evaluation indicate the potential to detect the effect of small geometrical defects in tensile and three-point bending specimens. Evaluation of the AE data based on signal strength was useful for understanding damage initiation and

progression. Conclusions are listed below.

1. Traditional response measurements including load–displacement curves or stiffness did not clearly show the effect of induced defects.
2. For tensile coupons, cumulative signal strength did not indicate the effect of defects when comparing each defect with pristine specimens of the same configuration.
3. Intensity Analysis charts provided insight to the level of potential damage (i.e. matrix cracking and delamination) occurring in the pristine and defect induced specimens under tensile loading.
4. Defect induced tensile specimens showed higher historic and severity indices than pristine specimens, indicating the potential for acoustic emission evaluation to better understand the effect of AFP defects.
5. Cumulative Signal Strength (CSS) clearly shows the effect of double defects induced in three-point bending specimens. Higher damage was observed earlier in defect induced specimens than in pristine specimens.
6. An acoustic emission 2D source localization algorithm describes damage progression of bending specimens and agrees with DIC images and load–displacement response.

Declaration of Competing Interest

The authors declare that they have no known competing financial interests or personal relationships that could have appeared to influence the work reported in this paper.

Acknowledgments

This material is based upon work supported by the National Aeronautics and Space Administration (NASA) under Award No. NNL09AA00A. Any opinions, findings, and conclusions expressed in this material are those of the author(s) and do not necessarily reflect the views of NASA. Also, special thanks to Brenna L. Feirer and David Bianco, research assistants at the mechanical and civil engineering departments-USC.

References

[1] AEwin version E4.30 [Computer software]. Princeton Junction, NJ, Mistras Group.
[2] Anay R, Cortez TM, Jáuregui DV, ElBatanouny MK, Ziehl P. On-site acoustic-emission monitoring for assessment of a prestressed concrete double-tee-beam bridge without plans. J Perform Constr Facil 2016;30(4):04015062. https://doi.org/10.1061/(ASCE)CF.1943-5509.0000810.
[3] Anay R, Lane A, Jáuregui DV, Weldon BD, Soltangharaei V, Ziehl P. On-site acoustic-emission monitoring for a prestressed concrete BT-54 AASHTO girder bridge. J Perform Constr Facil 2020;34(3):04020034. https://doi.org/10.1061/(ASCE)CF.1943-5509.0001440.
[4] Anay R, Ziehl P, Tessema A, Wehbe RY, Assi L, Kidane A, Gürdal Z. An Experimental Investigation Concerning the Effects of AFP Defects on Progressive Failure of Tensile Coupons. In AIAA Scitech 2019 Forum; 2019 (p. 1547).
[5] ASTM. Standard terminology for nondestructive examinations. E1316, West Conshohocken, PA; 2014.
[6] Azadi M, Sayar H, Ghasemi-Ghalebahman A, Jafari SM. Tensile loading rate effect on mechanical properties and failure mechanisms in open-hole carbon fiber reinforced polymer composites by acoustic emission approach. Compos B Eng 2019;158:448–58.
[7] Bader S. Crystic composites handbook. Wollaston: Scott Bader Company; 2005. p. 45.
[8] Barile M, Lecce L, Esposito M, D'Amato GM, Sportelli A. Advanced AFP applications on multifunctional composites. In: The Second International Symposium on Automated Composites Manufacturing. April; 2015. p. 23–4.
[9] Cantwell WJ, Morton J. The impact resistance of composite materials—a review. composites 1991;22(5):347–62.
[10] Clyne TW, Hull D, editors. An introduction to composite materials. Cambridge University Press; 2019.
[11] de Groot PJ, Wijnen PAM, Janssen RBF. Real-time frequency determination of acoustic emission for different fracture mechanisms in carbon/epoxy composites. Compos Sci Technol 1995;55(4):405–12.
[12] Di Francesco M, Giddings P, Potter K. On the layup of convex corners using Automated Fibre Placement: an evaluation method. In Proceedings of ACM2–International Symposium on Automated Composites Manufacturing, Montreal, CA; 2015.
[13] Ekanayake S, Gurram S, Schmitt RH. Depth determination of defects in CFRP-structures using lock-in thermography. Compos B Eng 2018;147:128–34.
[14] ElBatanouny MK, Ziehl PH, Larosche A, Mangual J, Matta F, Nanni A. Acoustic emission monitoring for assessment of prestressed concrete beams. Constr Build Mater 2014;58:46–53.
[15] Fowler T, Blessing J, Conlisk P. New directions in testing. In AECM-3: International Symposium on Acoustic Emission from Composite Materials, 3rd, Paris, France; 1989 (pp. 16–27).
[16] Girdauskaite L, Krzywinski S, Schmidt-Eisenlohr C, Krings M. Introduction of automated 3d vacuum buildup in the composite manufacturing chain. Paper presented at: The Second International Symposium on Automated Composites Manufacturing. 2015. 23-24 April.
[17] Golaski L, Gebski P, Ono K. Diagnostics of reinforced concrete bridges by acoustic emission. Journal of acoustic emission 2002;20(2002):83–9.
[18] Gurit, "Guide to Composites," http://www.gurit.com/guide-to-composites.aspx.
[19] Harik R, Saidy C, Williams SJ, Gurdal Z, Grimsley B. Automated fiber placement defect identity cards: cause, anticipation, existence, significance, and progression; 2018.
[20] Jonsson M, Eklund D, Järneteg A, Åkermo M, Sjölander J. Automated manufacturing of an integrated pre-preg structure. In: The Second International Symposium on Automated Composites Manufacturing. April; 2015. p. 23–4.
[21] Marani R, Palumbo D, Renò V, Galietti U, Stella E, D'Orazio T. Modeling and classification of defects in CFRP laminates by thermal non-destructive testing. Compos B Eng 2018;135:129–41.
[22] Mukhopadhyay S, Jones MI, Hallett SR. Compressive failure of laminates containing an embedded wrinkle; experimental and numerical study. Compos A Appl Sci Manuf 2015;73:132–42.
[23] Nair A, Cai CS. Acoustic emission monitoring of bridges: review and case studies. Eng Struct 2010;32(6):1704–14.
[24] Ning W. Structural health condition monitoring of carbon-fibre based composite materials using acoustic emission techniques (Doctoral dissertation. University of Birmingham); 2015.
[25] Oromiehie E, Prusty BG, Compston P, Rajan G. Automated fibre placement based composite structures: Review on the defects, impacts and inspections techniques. Compos Struct 2019;224:110987.
[26] Quddus, M., Brux, A., Larregain, B., & Galarneau, Y. (2015, April). A study to determine the influence of robotic lamination programs on the precision of automated fiber placement through statistical comparisons. In Proc. 2nd Int. Symp. Automated Composites Manuf. (pp. 23–24).
[27] Rajan S, Sutton MA, Wehbe R, Tatting B, Gürdal Z, Kidane A, et al. Experimental investigation of prepreg slit tape wrinkling during automated fiber placement process using StereoDIC. Compos B Eng 2019;160:546–57.
[28] Roberts TM, Talebzadeh M. Acoustic emission monitoring of fatigue crack propagation. J Constr Steel Res 2003;59(6):695–712.
[29] Rousseau G, Wehbe R, Halbritter J, Harik R. Automated fiber placement path planning: a state-of-the-art review. Comput-Aided Des Applic 2019;16(2):172–203.
[30] Saeedifar M, Saleh MN, El-Dessouky HM, De Freitas ST, Zarouchas D. Damage assessment of NCF, 2D and 3D woven composites under compression after multiple-impact using acoustic emission. Compos A Appl Sci Manuf 2020;132:105833.
[31] Wehbe R, Tatting B, Rajan S, Harik R, Sutton M, Gürdal Z. Geometrical modeling of tow wrinkles in automated fiber placement. Compos Struct 2020;246:112394.
[32] Wehbe R, Sacco C, Radwan AB, Albazzan M, Harik R. Influence of process parameters in AFP fiber steering on cylinders: constant curvature paths. Composites Part C 2020:100036. Open Access.
[33] Xu D, Liu PF, Chen ZP, Li JG, Leng JX, Zhu RH, et al. Delamination analysis of carbon fiber/epoxy composite laminates under different loading rates using acoustic emission. J Fail Anal Prev 2019;19(4):1034–42.
[34] Yong G, Denghong X, Tian H, Ye L, Naitian L, Quanhong Y, et al. Identification of damage mechanisms of carbon fiber reinforced silicon carbide composites under static loading using acoustic emission monitoring. Ceram Int 2019;45(11):13847–58.
[35] Zhou W, Zhang P-F, Yin H-F, Shang Y-J. Flexural damage behavior of carbon fiber three-dimensional braided composites using acoustic emission and micro-CT. Mater Res Express 2019;6(11):115601.